

---

---

# First-in-Humans Imaging with $^{89}\text{Zr}$ -Df-IAB22M2C Anti-CD8 Minibody in Patients with Solid Malignancies: Preliminary Pharmacokinetics, Biodistribution, and Lesion Targeting

Neeta Pandit-Taskar<sup>1-3</sup>, Michael A. Postow<sup>4,5</sup>, Matthew D. Hellmann<sup>3-5</sup>, James J. Harding<sup>4,5</sup>, Christopher A. Barker<sup>6</sup>, Joseph A. O'Donoghue<sup>7</sup>, Martha Ziolkowska<sup>1</sup>, Shutian Ruan<sup>1,2</sup>, Serge K. Lyashchenko<sup>8,9</sup>, Frank Tsai<sup>10</sup>, Michael Farwell<sup>11</sup>, Tara C. Mitchell<sup>11</sup>, Ron Korn<sup>12</sup>, William Le<sup>13</sup>, Jason S. Lewis<sup>1,8,9</sup>, Wolfgang A. Weber<sup>1</sup>, Deepak Behera<sup>13</sup>, Ian Wilson<sup>13</sup>, Michael Gordon<sup>10</sup>, Anna M. Wu<sup>13,14</sup>, and Jedd D. Wolchok<sup>3-5</sup>

<sup>1</sup>Department of Radiology, Memorial Sloan Kettering Cancer Center, New York, New York; <sup>2</sup>Department of Radiology, Weill Cornell Medical College, New York, New York; <sup>3</sup>Parker Institute for Cancer Immunotherapy, Memorial Sloan Kettering Cancer Center, New York, New York; <sup>4</sup>Department of Medicine, Memorial Sloan Kettering Cancer Center, New York, New York; <sup>5</sup>Department of Medicine, Weill Cornell Medical College, New York, New York; <sup>6</sup>Department of Radiation Oncology, Memorial Sloan Kettering Cancer Center, New York, New York; <sup>7</sup>Department of Medical Physics, Memorial Sloan Kettering Cancer Center, New York, New York; <sup>8</sup>Molecular Pharmacology Program, Memorial Sloan Kettering Cancer Center, New York, New York; <sup>9</sup>Radiochemistry and Molecular Imaging Probes Core, Memorial Sloan Kettering Cancer Center, New York, New York; <sup>10</sup>Honor Health, Scottsdale, Arizona; <sup>11</sup>University of Pennsylvania, Philadelphia, Pennsylvania; <sup>12</sup>Imaging Endpoints, Scottsdale, Arizona; <sup>13</sup>ImaginAb, Inc., Inglewood, California; and <sup>14</sup>Department of Molecular Imaging and Therapy, Beckman Research Institute of the City of Hope, Duarte, California

Immunotherapy is becoming the mainstay for treatment of a variety of malignancies, but only a subset of patients responds to treatment. Tumor-infiltrating CD8-positive (CD8+) T lymphocytes play a central role in antitumor immune responses. Noninvasive imaging of CD8+ T cells may provide new insights into the mechanisms of immunotherapy and potentially predict treatment response. We are studying the safety and utility of  $^{89}\text{Zr}$ -IAB22M2C, a radiolabeled minibody against CD8+ T cells, for targeted imaging of CD8+ T cells in patients with cancer. **Methods:** The initial dose escalation phase of this first-in-humans prospective study included 6 patients (melanoma, 1; lung, 4; hepatocellular carcinoma, 1). Patients received approximately 111 MBq (3 mCi) of  $^{89}\text{Zr}$ -IAB22M2C (at minibody mass doses of 0.2, 0.5, 1.0, 1.5, 5, or 10 mg) as a single dose, followed by PET/CT scans at approximately 1–2, 6–8, 24, 48, and 96–144 h after injection. Biodistribution in normal organs, lymph nodes, and lesions was evaluated. In addition, serum samples were obtained at approximately 5, 30, and 60 min and later at the times of imaging. Patients were monitored for safety during infusion and up to the last imaging time point. **Results:**  $^{89}\text{Zr}$ -IAB22M2C infusion was well tolerated, with no immediate or delayed side effects observed after injection. Serum clearance was typically biexponential and dependent on the mass of minibody administered. Areas under the serum time–activity curve, normalized to administered activity, ranged from 1.3 h/L for 0.2 mg to 8.9 h/L for 10 mg. Biodistribution was dependent on the minibody mass administered. The highest uptake was always in spleen, followed by bone marrow. Liver uptake was more pronounced with higher minibody masses. Kidney uptake was typically low. Prominent uptake was seen in multiple normal lymph nodes as early as 2 h after injection, peaking by 24–48 h after injection. Uptake in tumor lesions was seen on imaging as early as 2 h after injection, with most  $^{89}\text{Zr}$ -IAB22M2C–positive lesions

detectable by 24 h. Lesions were visualized early in patients receiving treatment, with SUV ranging from 5.85 to 22.8 in 6 target lesions. **Conclusion:**  $^{89}\text{Zr}$ -IAB22M2C imaging is safe and has favorable kinetics for early imaging. Biodistribution suggests successful targeting of CD8+ T-cell-rich tissues. The observed targeting of tumor lesions suggests this may be informative for CD8+ T-cell accumulation within tumors. Further evaluation is under way.

**Key Words:**  $^{89}\text{Zr}$ -IAB22M2C PET; minibody; CD8+ T cell; lung cancer; melanoma

**J Nucl Med 2020; 61:512–519**  
DOI: 10.2967/jnumed.119.229781

**I**mmunotherapy with checkpoint inhibitors has recently emerged as a useful treatment for a variety of solid tumors and select hematologic malignancies. The goals of immunotherapy include recruiting or increasing the activation of immune cells to enhance tumor killing. Tumor-infiltrating T cells play a central role in this process (1) and, in particular, CD8-positive (CD8+) T cells are important for initiating and mediating a response to CTLA-4 and anti-PD-1/PD-L1 checkpoint inhibitors (2–5). Although treatment with checkpoint inhibitors can be effective, responses are seen in only a subset of patients (6,7). Therefore, effective methods to select effective therapies and predict response would play a critical role in patient management. In particular, the ability to noninvasively visualize CD8+ T cells in vivo before and during treatment would represent a major advancement in our understanding of local and systemic immune responses and facilitate the development of more effective immune cell–targeted single or combination therapies.

IAB22M2C is an 80-kDa minibody (engineered single-chain variable-fragment–heavy-chain 3 antibody fragment) with high affinity to human CD8. IAB22M2C is a bivalent homodimer—with each monomer consisting of a single-chain variable fragment linked to the human IgG1 heavy-chain 3 domain engineered from

---

Received May 8, 2019; revision accepted Aug. 21, 2019.  
For correspondence or reprints contact: Neeta Pandit-Taskar, Memorial Sloan Kettering Cancer Center, 1275 York Ave., New York, NY 10065.  
E-mail: pandit-n@mskcc.org  
Published online Oct. 4, 2019.  
COPYRIGHT © 2020 by the Society of Nuclear Medicine and Molecular Imaging.

the humanized heavy- and light-chain sequences of murine anti-human OKT8 antibody—and targets human CD8 with high affinity (binding half-maximal effective concentration, 0.4 nM). The minibody is fully humanized and lacks a heavy-chain 2 domain, resulting in a protein that is biologically inert and therefore does not interact with Fc- $\gamma$ -receptors or the neonatal Fc recycling receptor. Combined with the reduced molecular weight of the minibody, these modifications produce an antibody fragment with accelerated serum clearance, favorable for in vivo imaging (8,9).

Preclinical studies of IAB22M2C and desferrioxamine-conjugated IAB22M2C showed retention of high-affinity binding to human T cells and HPBALL leukemia cells. Incubation with peripheral blood mononuclear cells from healthy human donors showed no measurable impact on proliferation or depletion of CD8+ T cells, nor was induction of cytokines shown when donor cells were exposed to immobilized protein. In vivo studies on humanized NSG mice (The Jackson Laboratory) engrafted with CD34+ stem cells showed no acute effects of Df-IAB22M2C on CD8+ T-cell populations, nor was cytokine release shown after intravenous administration. For full-sized antibodies, optimal lesion detection typically occurs 4–8 d after injection (10). Smaller minibodies have faster clearance, leading to high tumor-to-background ratios at earlier times and the feasibility of early imaging (11–13).

Df-IAB22M2C was radiolabeled with  $^{89}\text{Zr}$  for immuno-PET studies on a humanized mouse model of graft-versus-host disease, demonstrating the ability to visualize infiltrating human CD8+ T cells in affected organs (14). These and other studies supported the successful filing of an investigational new drug application for current-good-manufacturing-practice production and  $^{89}\text{Zr}$  labeling of Df-IAB22M2C for clinical evaluation.

Here, we provide a preliminary report on this evaluation of  $^{89}\text{Zr}$ -IAB22M2C imaging in the first 6 patients with solid tumors who were either undergoing or likely to undergo immunotherapy.

## MATERIALS AND METHODS

A prospective phase I open-label, nonrandomized dose-escalation imaging study with  $^{89}\text{Zr}$ -IAB22M2C was performed on patients with various malignancies. Eligible tumors included small cell or non-small cell lung cancer, squamous cell carcinoma of the head and neck, melanoma, Merkel cell carcinoma, renal cell carcinoma, bladder cancer, hepatocellular carcinoma, triple-negative breast cancer, gastroesophageal cancers, and Hodgkin lymphoma. The protocol was Institutional Review Board–approved, and all patients provided written informed consent (ClinicalTrials.gov identifier NCT03107663).

All patients had histologically confirmed malignancies with at least 1 measurable lesion and were either on immunotherapy or were eligible to receive immunotherapy. All underwent baseline imaging, including CT or MRI performed as the standard of care within 4 wk of  $^{89}\text{Zr}$ -IAB22M2C administration. The total IAB22M2C mass dose was escalated, starting with 0.2 mg and increasing to 0.5, 1.0, 1.5, 5.0, and 10 mg in 1 patient each consecutively for the first 6 patients. All patients underwent serial imaging for biodistribution and multiple blood sampling for pharmacokinetic analysis.

### $^{89}\text{Zr}$ -IAB22M2C Minibody Formulation and Injection

IAB22M2C minibody, obtained from ImaginAb, Inc., was conjugated to good-manufacturing-practice–grade desferrioxamine B from Macrocyclics in the Radiochemistry and Molecular Imaging Core at Memorial Sloan Kettering Cancer Center (MSK). Sterile Df-IAB22M2C was stored at 4°C for up to 2 wk before radiolabeling.  $^{89}\text{Zr}$  production and subsequent radiolabeling of Df-IAB22M2C were performed as previously described (15–17). Approximately 0.2–1 mg

of Df-IAB22M2C was labeled with  $^{89}\text{Zr}$  and purified by a PD-10 column. The final product was supplemented with cold IAB22M2C minibody and diluted with formulation buffer, as needed. Before release, the final radiolabeled product was tested for appearance, pH, radiochemical identity, and purity by size-exclusion high-performance liquid chromatography and instant thin-layer chromatography; for radiochemical purity by  $\gamma$ -spectroscopy; for endotoxin level by a portable test system reader; and for immunoreactivity by the bead method. Sterility testing was performed after release. The radiolabeling efficiency was more than 80%, radiochemical purity was more than 95% as determined by instant thin-layer chromatography, and minibody binding was more than 90%.

### $^{89}\text{Zr}$ -IAB22M2C Administration

The radiolabeled minibody, in combination with cold Df-IAB22M2C to make up the designated total mass balance, was administered intravenously over 5–10 min. No premedications were administered. Patients were monitored up to the time of imaging (2–4 h or 6–8 h after injection) for vital signs and any side effects and 24 h later for any reactions or adverse events. Side effects and reactions were graded per the Common Terminology Criteria for Adverse Events, version 4.0.

### PET Imaging

PET/CT images were acquired at 2 centers using either a Discovery 710 or a Discovery STE scanner (GE Healthcare). Each patient underwent 4–5 whole-body PET/CT scans from vertex of skull to feet at 2–4 h, 24  $\pm$  4 h, 48  $\pm$  4 h, and 92–148 h after injection. Patients had the option of undergoing an additional scan at 6–8 h after injection. Emission scans were acquired in 3-dimensional mode at variable times per field of view (3 min on the day of injection, extending to 7 min at 92–148 h). PET/CT was performed using low-dose CT for attenuation correction, with a single low-dose CT scan at 24 h being obtained with a 80-mA tube current (120 kVp; estimated radiation dose, 9.0 mGy). All other low-dose CT scans were done with 10-mA current (120 kVp; estimated radiation dose, 1.1 mGy). Images were reconstructed with a 70-cm field of view into a 128  $\times$  128 matrix using iterative ordered-subset expectation maximization (16 subsets; 2 iterations). All corrections recommended by the manufacturer were applied.

### Uptake in Normal Tissues and Lesions

Images were viewed for sites of  $^{89}\text{Zr}$ -IAB22M2C uptake. Volumes of interest were drawn within normal organs or tissues, including heart, lung, liver, spleen, bone marrow, nodes, and kidney, as well as tumor lesions, using dedicated software (Hermes Medical Solutions). A site of uptake that did not conform to normal expected biodistribution and was clearly above the adjacent normal background activity was considered positive for a tumor lesion. A subset of index lesions (maximum of 2 lesions per patient) was analyzed for uptake trends. SUV was quantified using either SUV<sub>mean</sub> (normal tissues) or SUV<sub>max</sub> (lesions) normalized to lean body mass (SUV<sub>LBM</sub>) (18).

### Serum Clearance Measurements

Multiple blood samples were obtained for assessment, including a baseline sample before  $^{89}\text{Zr}$ -IAB22M2C infusion, followed by sampling at 5, 30, 60, and 120–240 min after injection and subsequently at the time of each PET scan, totaling 7–8 samples. Samples were measured in duplicate using a NaI(Tl)  $\gamma$ -well-type detector (Wallac Wizard 1480 automatic  $\gamma$ -counter; Perkin Elmer) together with appropriate standards. The measured activity concentrations were converted to percentage injected activity per liter.

### Derivation of Whole-Body and Serum Clearance

To visualize trends in biodistribution and pharmacokinetics, we examined the time course of whole-body and serum activity clearance together with SUV for normal tissues and lesions.

## RESULTS

In total, 6 patients were imaged in this initial dose escalation phase (Table 1). Injections were tolerated well, with no infusion reactions. No adverse events were observed over the study period. The mean injected activity was 108 MBq (2.91 mCi), with a range of 92–120 MBq (2.5–3.25 mCi). The radiolabeled antibody mass was 0.12 mg for the 0.2-mg dose level; for other levels, the mean ( $\pm$ SD) mass was 0.34 ( $\pm$ 0.02) mg.

### Biodistribution

Prominent activity was seen in spleen, bone marrow, and liver in all patients, with the highest uptake being seen in spleen, followed by marrow. Blood-pool activity was negligible at the lowest minibody mass and was more prominent at earlier and later time points with higher minibody mass (Fig. 1). Uptake in liver was noted in all patients, and gastrointestinal tract activity (on average, 4.5% of injected activity) was seen up to 48 h after injection. The gallbladder was frequently visualized at the earliest times, with peak activity on the first or second day. Renal uptake varied among patients but was primarily cortical and tended to plateau beyond 48 h. No significant bladder activity was seen except in 1 patient (1.0 mg), in whom activity was clearly seen in the urinary bladder in both of the early scans. The biodistribution of  $^{89}\text{Zr}$ -IAB22M2C was highly dependent on minibody mass (Fig. 2). At the lowest mass dose (0.2–0.5 mg), uptake was almost completely confined to the spleen and, to a lesser extent, bone marrow and lymph nodes, with little or no apparent blood-pool activity even at the earliest times after injection. As the mass dose increased, blood-pool retention increased and the biodistribution showed higher liver uptake at later times. However, spleen uptake remained dominant at all times for all minibody masses examined.

### Serum and Whole-Body Kinetics

Serum clearance was biexponential and dependent on the mass of minibody administered. At lower masses (0.2–1.5 mg), activity in the serum cleared rapidly (Fig. 3A). The effective half-times were 0.3–10.6 h for the fast component and 26.4–102.7 h for the slow component.

**TABLE 1**  
Patient Demographics

Demographic	Data
Total patients ( <i>n</i> )	6
Age range (y)	38–81
Sex ( <i>n</i> )	
Male	3
Female	3
Primary malignancy ( <i>n</i> )	
Melanoma	1
Hepatocellular carcinoma	1
Lung	4
Treatment profile for current immunotherapy ( <i>n</i> )	
None	1
Current < 1 mo from imaging	1
Current > 6 mo from imaging	2
Prior > 6 mo from imaging	2

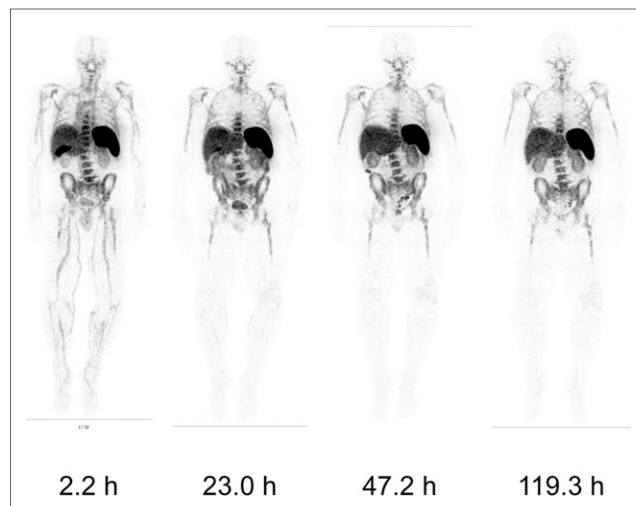


**FIGURE 1.** Biodistribution: Whole-body images of 1 patient at various times after injection of  $^{89}\text{Zr}$ -IAB22M2C (1.5-mg minibody dose). All images show most intense activity within spleen, followed by marrow, liver, and kidneys.

Whole-body clearance generally conformed to monoexponential kinetics, with the exception of the 1.0-mg minibody mass, for which clearance was distinctly biexponential (Fig. 3B). The median whole-body biologic half-life was 235 h (range, 123–288 h) and had no obvious relationship to minibody mass, apart from the idiosyncratic fast clearance in the patient receiving the 1.0-mg dose.

### Uptake in Normal Tissues

The spleen showed the highest uptake in all patients at all minibody dose levels, but with a consistent pattern of decreasing uptake at higher cold minibody masses (Figs. 2 and 4A–4D). For low minibody masses, spleen uptake was maximal in the earliest

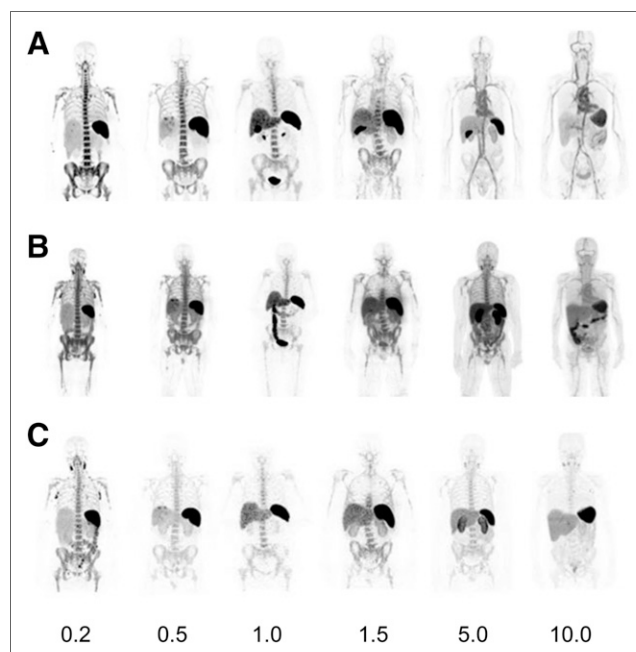


**FIGURE 2.** Biodistribution and normal-organ uptake in 6 patients at 2–4 h (A), 24 h (B), and 92–148 h (C) after injection of  $^{89}\text{Zr}$ -IAB22M2C (0.2- to 10.0-mg minibody dose).

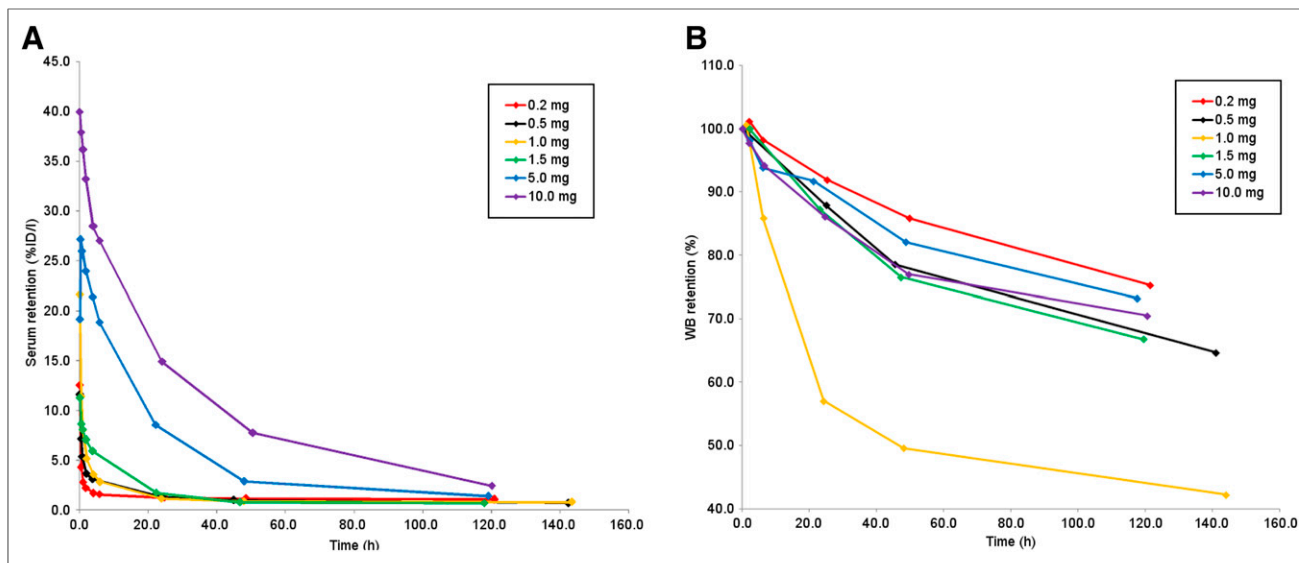


**FIGURE 3.** Serum (A) and whole-body clearance (B) of  $^{89}\text{Zr}$ -IAB22M2C at various mass levels, in aggregate mean values of decay-corrected activity retention. %ID = percentage injected dose; WB = whole body.

images and subsequently decreased, whereas for the 2 highest masses (5 and 10 mg), maximal uptake occurred at about 24 h. The range of splenic  $\text{SUV}_{\text{LBM}}$  (Fig. 4A) extended from 10.5 for the 10-mg dose to 50 for the 0.2-mg dose. Bone marrow showed the second highest uptake, peaking in most patients by 6–24 h. Marrow uptake was also

highly dependent on minibody mass, with  $\text{SUV}_{\text{LBM}}$  ranging from 1.8 to 8.6 for 10 mg to 0.2 mg, respectively (Fig. 4B). Liver uptake was significantly lower than spleen uptake and was generally highest at the earlier times of imaging on day 1 or within 24 h. Liver uptake generally either decreased mildly or plateaued over 48–120 h

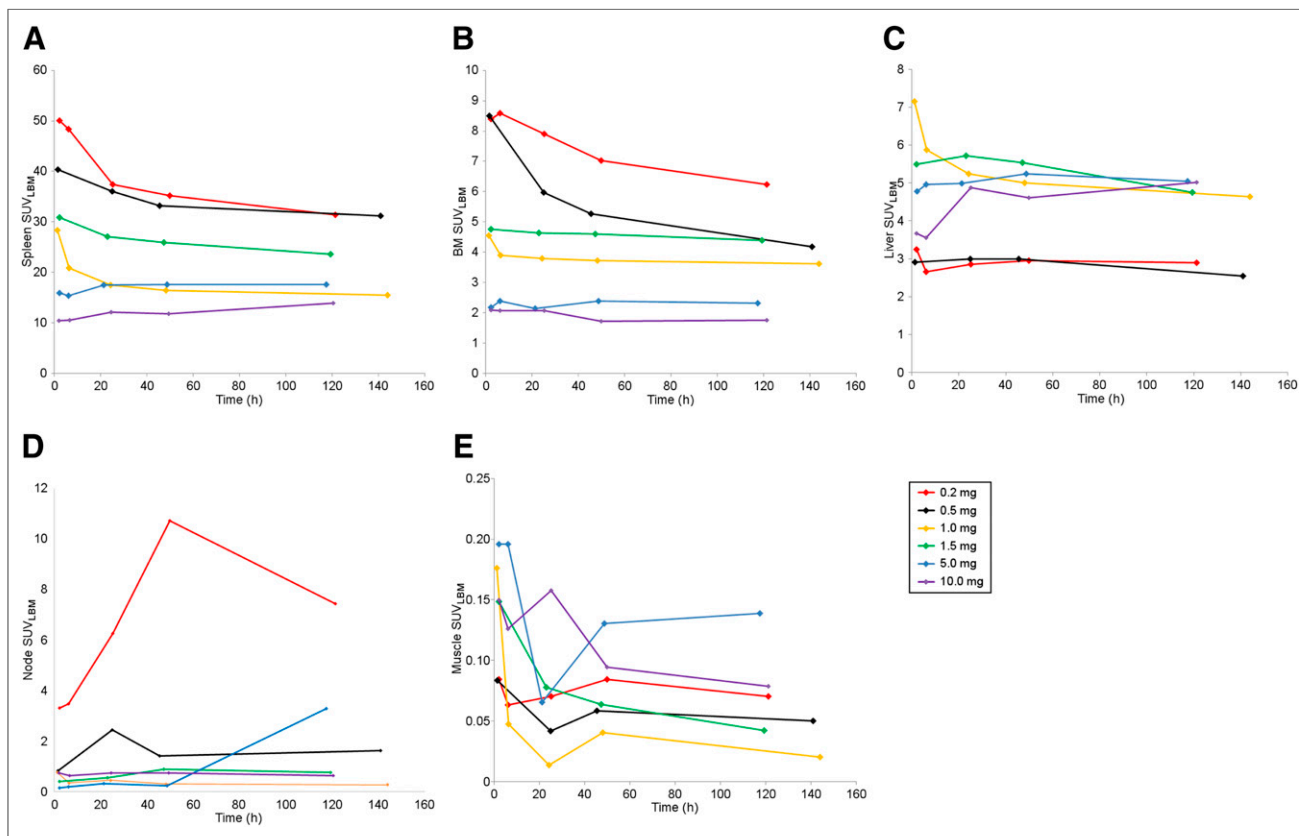


**FIGURE 4.** Normal-organ uptake (mean  $\text{SUV}_{\text{LBM}}$ ) in spleen (A), marrow (B), liver (C), nodes (D), and muscle (background uptake) (E) vs. minibody mass. BM = bone marrow.

and showed higher uptake at larger masses (1.0 mg or above) (Fig. 4C). Multiple normal nodes were seen in all patients at all dose levels except 1 mg. The greatest number of nodes and the highest nodal uptake were noted at 0.2 mg, subsequently decreasing as minibody mass increased (Fig. 4D). Nodal uptake increased within the first 24–48 h in most patients, though it did not increase substantially at higher masses. At both the 0.2- and the 0.5-mg levels, multiple nodes were prominently seen even at the earliest imaging times (2–6 h after injection). Normalized uptake in organs in relation to muscle uptake is separately provided in Supplemental Figure 1 (supplemental materials are available at <http://jnm.snmjournals.org>).

#### Uptake in Metastatic Lesions

Metastatic lesion uptake was prominent in 2 patients (1 melanoma and 1 hepatocellular carcinoma) imaged at the 0.2- and 0.5-mg dose levels, respectively. Both patients were receiving immunotherapy. Lesion uptake was seen as early as 2 h after injection and gradually increased with delayed imaging; the highest uptake in most lesions was seen at 24 or 48 h. One hepatic metastasis showed the highest uptake at the 2- to 4-h imaging. The patient with melanoma showed uptake in a deltoid muscle metastasis with an SUV of 1.4 that was also  $^{18}\text{F}$ -FDG-avid and found to have peritumoral and intratumoral CD8 T-cell infiltration after surgical excision of the lesion for clinical reasons (Fig. 5). The hepatocellular carcinoma patient had uptake in 2 liver metastases ( $\text{SUV}_{\text{max}}$ , 14.6 and 22.85) and additional uptake in 3 abdominal lymph node metastases ( $\text{SUV}_{\text{max}}$ , 5.85–10.9) (Fig. 6). No significant uptake of  $^{89}\text{Zr}$ -IAB22M2C was seen in 4 patients with lung metastases ( $\text{SUV}$ , 0.3–1.2).

The uptake in tumors by directed imaging of CD8+ T cells with  $^{89}\text{Zr}$ -IAB22M2C PET was both concordant and discordant with  $^{18}\text{F}$ -FDG PET. In the melanoma patient, the lesions were positive on both  $^{89}\text{Zr}$ -IAB22M2C and  $^{18}\text{F}$ -FDG PET (Fig. 5). Among the 4 patients negative for  $^{89}\text{Zr}$ -IAB22M2C uptake in lesions, a lung metastasis in 1 patient demonstrated  $^{18}\text{F}$ -FDG avidity (Fig. 7), whereas the other 3 patients had no  $^{18}\text{F}$ -FDG uptake in any lesions. All 4 patients either had not initiated immunotherapy ( $n = 1$ ), had received immunotherapy in the past more than 6 mo before imaging ( $n = 2$ ), or had been receiving immunotherapy (nivolumab) for about 2 y ( $n = 1$ ). The  $^{89}\text{Zr}$ -IAB22M2C-negative lesions included nodes (1.7–4.0 cm), a soft-tissue lesion (3.3 cm), a liver lesion (3.7 cm), and lung nodules (0.5–4.7 cm) (Fig. 7).

#### DISCUSSION

Immune-modulating checkpoint blockade therapies are increasingly playing a critical role in the treatment of several cancers. Although they are being used in the treatment of several cancers and across specific patient populations, response is seen in only a subset of patients. A key determinant of successful therapy is the presence of CD8+ T cells that modulate the immune response. Current methods of assessing CD8+ T-cell infiltration by tumor biopsy are invasive and may not always be practical or available. Additionally, tumor biopsies assess only the single site of sampled disease, which may be problematic given immunologic heterogeneity among multiple tumors within an individual patient (19). A noninvasive method of imaging that can accurately allow for assessment of CD8+ T cells in tumors would be extremely useful in clinical research and patient management to better determine the effectiveness of therapy.

This was a first-in-humans study using  $^{89}\text{Zr}$ -IAB22M2C, a novel and unique minibody that is highly specific for targeting CD8+ T cells and shows clinical feasibility in PET/CT imaging. We evaluated  $^{89}\text{Zr}$ -IAB22M2C PET imaging as a means to assess CD8+ T-cell distribution in normal and malignant tissues and studied its distribution and kinetics in patients with a variety of malignancies. In this unique, noninvasive whole-body PET study,  $^{89}\text{Zr}$ -IAB22M2C was found to be easy to administer and well tolerated, with no observed infusion-related side effects for any minibody mass level up to 10 mg.

The biodistribution of  $^{89}\text{Zr}$ -IAB22M2C strongly suggests that it targets CD8+ T-cell-enriched tissues; notably high uptake was seen in spleen, bone marrow, and lymph nodes. The time course of activity in gallbladder and gastrointestinal tract was consistent with metabolic excretion via the hepatobiliary pathway, as noted for other  $^{89}\text{Zr}$ -labeled minibodies (13). Liver and kidneys were other tissues with notable uptake, with accumulation in kidney primarily confined to the renal cortex. However, in 1 patient who received a 1.0-mg minibody mass, there was early urinary clearance with significant activity in the urinary bladder at

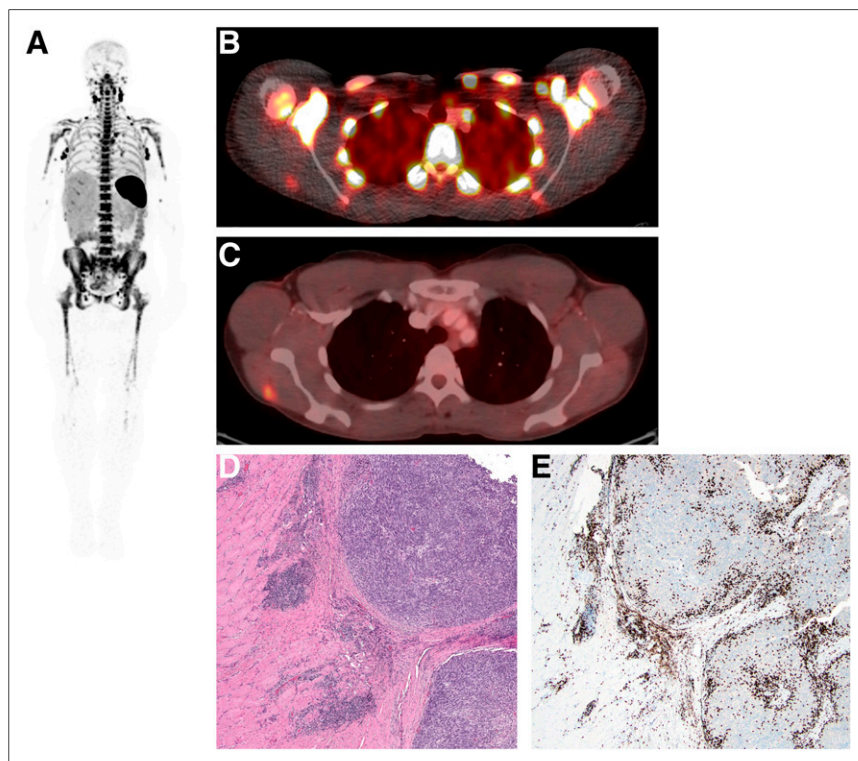


**FIGURE 5.** A 24-h whole-body (maximum-intensity projection) image in patient imaged with 0.2 mg of  $^{89}\text{Zr}$ -IAB22M2C. (A) Intense uptake is noted in lymph nodes. (B and C) Fusion image at 24 h shows  $^{89}\text{Zr}$ -IAB22M2C uptake in lesion in deltoid (B), which was also  $^{18}\text{F}$ -FDG-positive (C). (D) Hematoxylin- and eosin-stained section shows melanoma tumor nodules on right within skeletal muscle. (E) Immunohistochemistry highlights presence of CD8+ T cells at periphery and infiltrating tumor.



**FIGURE 6.** Whole-body (maximum-intensity projection) image (left) and  $^{89}\text{Zr}$ -IAB22M2C (0.5 mg) images (right) of patient with hepatocellular carcinoma.  $^{89}\text{Zr}$ -IAB22M2C-positive lesions are seen in 2 liver metastases ( $\text{SUV}_{\text{max}}$ , 14.6 and 22.85), and additional uptake is seen in 3 abdominal lymph node metastases ( $\text{SUV}_{\text{max}}$ , 5.85–10.9).

both the 2- to 4-h and the 6- to 8-h time points. This observation, coupled with an unusual whole-body clearance curve that was distinctly biphasic, is considered to be idiosyncratic. The exact reason for this observation is unknown, and uptake patterns in normal tissues such as bone marrow and spleen in this patient exhibited a pattern similar to that in other patients, with good uptake in the CD8+ T-cell-rich tissue.

These initial data indicate that the minibody mass influences biodistribution and that targeting of CD8+ T-cell-rich tissues such as spleen, bone marrow, and nodes was affected by the minibody mass dose, being highest at the lowest mass (0.2 mg) and lowest at the highest mass (10 mg). This finding suggests a saturation effect

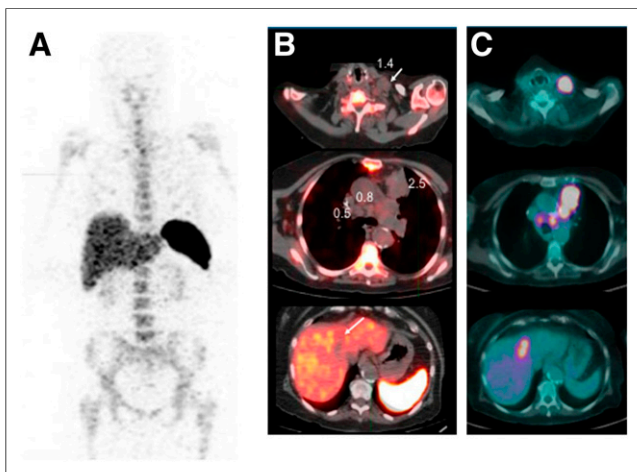


**FIGURE 7.** Whole-body (maximum-intensity projection) image (A),  $^{89}\text{Zr}$ -IAB22M2C (1.0 mg) images (B), and  $^{18}\text{F}$ -FDG images (C) of patient with lung cancer not initiated on immunotherapy. Lesions that are  $^{18}\text{F}$ -FDG-positive in left neck ( $\text{SUV}_{\text{max}}$ , 17.8; 3.2 cm), mediastinum ( $\text{SUV}_{\text{max}}$ , 11.1; 2.2 cm), left upper lobe ( $\text{SUV}_{\text{max}}$ , 20.4; 4.7 cm), and liver ( $\text{SUV}_{\text{max}}$ , 11.6; 3.7 cm) show no uptake of  $^{89}\text{Zr}$ -IAB22M2C.

due to competitive binding between the increasing amount of cold minibody and the radiolabeled  $^{89}\text{Zr}$ -IAB22M2C. This suggestion is supported by the serum clearance data, which show rapid extraction of lower minibody masses from the circulation, whereas slower clearance and higher retention were seen for higher minibody masses (5–10 mg). As the minibody mass increases, accessible antigen sites are saturated, more minibody remains in the circulation, and accumulation in the liver gradually increases.

Most radiolabeled minibody appeared to be stably bound to CD8+ T-cell-rich tissues over the duration of measurements, as indicated by the lack of any effect of increasing minibody mass on whole-body clearance of activity. The inverse relationship between liver uptake and minibody mass is unclear but may be affected by longer clearance times. The overall serum clearance was rapid for  $^{89}\text{Zr}$ -IAB22M2C, as noted for other minibodies (Fig. 3) (13), allowing for earlier optimal localization in normal tissues as well as prominent lesion detection within 6–24 h after injection (Figs. 5 and 6).

Multiple-time-point imaging showed variable trends in uptake and retention pattern in different tissues, with stable uptake in CD8+ tissues and clearance of blood-pool and background activity over time. CD8+ T-cell-rich tissues (spleen and marrow) showed the most prominent and stable uptake with time, with high uptake at early times at low minibody masses that tended to plateau beyond 24-h imaging and high retention even at later time points, suggesting minimal recirculation or excretion. Nodal uptake and visualization varied in time with minibody mass change, with more nodes seen at early time points (6–24 h after injection) at lower masses than at higher masses (5 or 10 mg), suggesting a strong effect of competitive binding of the cold minibody. However, there was an exception seen at the 1-mg level, at which lymph nodes did not show significant uptake, possibly related to lower binding due to faster clearance seen in this particular patient. Increased minibody binding to cells, along with greater clearance of activity from blood and background tissues at later time points, allows for better detection of nodes. The assessment of optimal mass and time for imaging based on the initial results of visual assessment and uptake patterns in tissues and lesions shows that imaging at 24 h after injection provides good visualization of both normal and tumor tissues that may be rich in CD8+ T cells. In this report on Tumor lesions showed variable uptake of  $^{89}\text{Zr}$ -IAB22M2C in patients, possibly related to the treatment profile or the variable presence of CD8+ T cells. High and early  $^{89}\text{Zr}$ -IAB22M2C uptake was noted in lesions in 2 patients imaged at lower masses (0.2 and 0.5 mg). These patients were receiving immunotherapy with pembrolizumab and nivolumab (0.2 and 0.5 mg, respectively), suggesting possible modulation of tumor-infiltrating T cells, leading to a higher concentration of CD8+ T cells and therefore prominent visualization by  $^{89}\text{Zr}$ -IAB22M2C PET/CT imaging. In 1 patient, histology and immunohistochemistry confirmed suspected CD8+ T-cell infiltration in a lesion that had uptake of  $^{89}\text{Zr}$ -IAB22M2C. Three patients with metastatic lung cancer did not show prominent uptake. Although the exact status of tumor-infiltrating T cells is not known because of the absence of parallel biopsy data, we postulate that the lack of prominent uptake in these patients may be related to a lack of ongoing treatment with immunotherapy and therefore low tumor-infiltrating T cells. It is also possible that the tumors did not have active disease, as all tumors were also not avid on  $^{18}\text{F}$ -FDG scan.

$^{89}\text{Zr}$ -IAB22M2C PET and  $^{18}\text{F}$ -FDG PET were concordant in the patient with melanoma (both positive; Fig. 5) and in 3 patients with lung cancer (both negative). In 1 patient, for whom immunotherapy

was not initiated,  $^{18}\text{F}$ -FDG was positive whereas  $^{89}\text{Zr}$ -IAB22M2C was negative, possibly because tumor-infiltrating T cells had not been stimulated at the time of  $^{89}\text{Zr}$ -IAB22M2C imaging (Fig. 6). This finding suggests that  $^{89}\text{Zr}$ -IAB22M2C uptake is independent of other processes such as enhanced permeability and vascular flow, potentially leading to nonspecific uptake in viable tumors.

Because of the small number of patients and variability in tumor types and treatment profiles, differences in lesion uptake among minibody mass doses cannot be established at this time. Our limited assessment suggests a more favorable balance of normal tissue and lesion visualization at lower minibody masses (less than 5 mg). Further analysis is ongoing in additional patients at different mass levels to further establish the role of minibody mass in imaging and dosimetry.

## CONCLUSION

This first-in-humans study showed that PET imaging with  $^{89}\text{Zr}$ -Df-IAB22M2C is safe, feasible, and well tolerated. The data support the ability of  $^{89}\text{Zr}$ -IAB22M2C minibody to successfully target CD8+ T-cell-rich tissues.  $^{89}\text{Zr}$ -IAB22M2C imaging has favorable kinetics for early imaging within 6–24 h after injection. Further evaluation is under way in more patients, and a study incorporating parallel biopsies is accruing patients.

## DISCLOSURE

This research was supported by ImaginAb, Inc., the Parker Institute for Cancer Immunotherapy, and the Radiochemistry and Molecular Imaging Probe Core of MSK, supported by NIH/NCI Cancer Center Support Grant P30 CA008748. Neeta Pandit-Taskar serves as a consultant to Y-mAbs Therapeutics, Inc., and has served on the advisory board of Progenics, Bayer, and Actinium Pharma. She has received honoraria from MedImmune/AstraZeneca. She receives or has received research support from Imaginab, Genentech, and Actinium Pharma. Michael Postow has received consulting fees from Bristol-Myers Squibb, Merck, Array BioPharma, Novartis, Incyte, NewLink Genetics, and Aduro Biotech (2015–present); honoraria from Bristol-Myers Squibb and Merck; and institutional support from Rgenix Inc., Infinity, Bristol-Myers Squibb, Merck, Array BioPharma, Novartis, and AstraZeneca. Matthew Hellmann receives research funding from Bristol-Myers Squibb; is a paid consultant to Merck, Bristol-Myers Squibb, AstraZeneca, Genentech/Roche, Janssen, Nektar, Syndax, Mirati, and Shattuck Labs; and has received travel support/honoraria from AstraZeneca and BMS. A patent has been filed by MSK related to the use of tumor mutation burden to predict response to immunotherapy (PCT/US2015/062208), which has received licensing fees from PGDx. James Harding has received research support and consulting fees from Bristol-Meyers Squibb and consulting fees from Eli Lilly and Company, CytomX Therapeutics, and Eisai Co., Ltd. Christopher Barker has received research funding for studies he is leading through his institution within the past year from Merck, Amgen, and Elekta, as well as for a study he is participating in from Bristol-Myers Squibb. He served as an unpaid member of an advisory board for Regeneron within the past year and as a paid member of an advisory board for Pfizer and Novartis over 2 years ago. Tara Mitchell has received honoraria from Merck, Bristol-Myers Squibb, Incyte, Regeneron, and Aduro. With regard to this publication, Jason Lewis' laboratory has received research support from ImaginAb, Inc. Anna Wu is a board member and consultant to ImaginAb, Inc. Jedd Wolchok reports personal fees from Adaptive Biotech, Advaxis, Amgen, Apricity, Array BioPharma,

Ascentage Pharma, Astellas, Bayer, Beigene, Celgene, Chugai, Elucida, Eli Lilly, F Star, Imvaq, Janssen, Kleo Pharma, Linneaus, Merck, Neon Therapeutics, Ono Pharmaceuticals, Polaris Pharma, Polynoma, Psioxus, Puretech, Recepta, Sellas Life, Seramatrix, Surface Oncology, Syndax, and Esanex and grants and personal fees from Bristol Myers Squibb, Genentech, and MedImmune outside the submitted work. In addition, Jedd Wolchok has pending patents for “Xenogeneic DNA Vaccines” (with royalties paid to Merial), “Alphavirus Replicon Particles Expressing TRP2,” “Newcastle Disease Viruses for Cancer Therapy,” “Genomic Signature to Identify Responders to Ipilimumab in Melanoma,” “Engineered Vaccinia Viruses for Cancer Immunotherapy” (to Imvaq), “Anti-CD40 Agonist mAb Fused to Monophosphoryl Lipid A (MPL) for Cancer Therapy”, and “CAR+ T Cells Targeting Differentiation Antigens as Means to Treat Cancer”. He also has the following patents: “Myeloid-Derived Suppressor Cell (MDSC) Assay” (with royalties paid to Seramatrix), “Anti-PD1 Antibody” (licensed to Agenus), “Anti-GITR Antibodies and Methods of Use Thereof” (licensed to Agenus/Incyte), and “Anti-CTLA4 Antibodies” (licensed to Agenus). Jedd Wolchok also has equity in Potenza Therapeutics, Tizona Pharmaceuticals, Adaptive Biotechnologies, Elucida, Imvaq, Beigene, Trieza, and Linneaus. Additionally, The Parker Institute is a shareholder of ImaginAb and has partnered with ImaginAb to directly support this clinical research at MSK. No other potential conflict of interest relevant to this article was reported.

## ACKNOWLEDGMENTS

We thank Antoni Ribas and Suzanne Topalian for their early contributions to the concept of this study. We also want to posthumously acknowledge Jean Gudas for her contributions to the development of the agent. We thank Dr. Maria Cecilia Lezcano Lopez in MSK's Department of Pathology for providing us with the pathology images of immunohistochemistry and hematoxylin- and eosin-stained tissues.

## KEY POINTS

**QUESTION:** Is it feasible to noninvasively visualize CD8 T cells with  $^{89}\text{Zr}$ -IAB22M2C?

**PERTINENT FINDINGS:** This phase I study evaluated the safety, feasibility, and optimal mass dose of imaging with a novel anti-CD8 minibody ( $^{89}\text{Zr}$ -IAB22M2C) and performed a preliminary evaluation of the ability of  $^{89}\text{Zr}$ -IAB22M2C to target CD8+ T-cell-rich tissues in patients with a variety of solid tumors. Preliminary data are encouraging, as  $^{89}\text{Zr}$ -IAB22M2C was safe and allowed early imaging of CD8+ T-cell-rich tissues at 24 h after injection. A phase II study to evaluate the concordance of  $^{89}\text{Zr}$ -IAB22M2C imaging with CD8+ T-cell presence by standard histologic assessment in patients receiving immunotherapy is under way.

**IMPLICATIONS FOR PATIENT CARE:** If proven in subsequent studies,  $^{89}\text{Zr}$ -IAB22M2C imaging has the potential to noninvasively assess the presence of CD8+ T cells in patients' tumors, which may ultimately serve as a biomarker of immunotherapy outcome and inform clinical trials of novel immunotherapies that act mechanistically through the presence of CD8+ T cells.

## REFERENCES

1. Gooden MJ, de Bock GH, Leffers N, Daemen T, Nijman HW. The prognostic influence of tumour-infiltrating lymphocytes in cancer: a systematic review with meta-analysis. *Br J Cancer*. 2011;105:93–103.

2. Azimi F, Scolyer RA, Rumcheva P, et al. Tumor-infiltrating lymphocyte grade is an independent predictor of sentinel lymph node status and survival in patients with cutaneous melanoma. *J Clin Oncol.* 2012;30:2678–2683.
3. Brahmer JR. PD-1-targeted immunotherapy: recent clinical findings. *Clin Adv Hematol Oncol.* 2012;10:674–675.
4. Tumeh PC, Harview CL, Yearley JH, et al. PD-1 blockade induces responses by inhibiting adaptive immune resistance. *Nature.* 2014;515:568–571.
5. Ribas A, Dummer R, Puzanov I, et al. Oncolytic virotherapy promotes intratumoral T cell infiltration and improves anti-PD-1 immunotherapy. *Cell.* 2018;174:1031–1032.
6. Brahmer JR, Tykodi SS, Chow LQ, et al. Safety and activity of anti-PD-L1 antibody in patients with advanced cancer. *N Engl J Med.* 2012;366:2455–2465.
7. Topalian SL, Hodi FS, Brahmer JR, et al. Safety, activity, and immune correlates of anti-PD-1 antibody in cancer. *N Engl J Med.* 2012;366:2443–2454.
8. Tavaré R, Escuin-Ordinas H, Mok S, et al. An effective immuno-PET imaging method to monitor CD8-dependent responses to immunotherapy. *Cancer Res.* 2016;76:73–82.
9. Tavaré R, McCracken MN, Zettlitz KA, et al. Engineered antibody fragments for immuno-PET imaging of endogenous CD8+ T cells in vivo. *Proc Natl Acad Sci USA.* 2014;111:1108–1113.
10. Pandit-Taskar N, O'Donoghue JA, Durack JC, et al. A phase I/II study for analytic validation of <sup>89</sup>Zr-J591 immunoPET as a molecular imaging agent for metastatic prostate cancer. *Clin Cancer Res.* 2015;21:5277–5285.
11. Knowles SM, Wu AM. Advances in immuno-positron emission tomography: antibodies for molecular imaging in oncology. *J Clin Oncol.* 2012;30:3884–3892.
12. Olafsen T, Sirk SJ, Olma S, Shen CK, Wu AM. ImmunoPET using engineered antibody fragments: fluorine-18 labeled diabodies for same-day imaging. *Tumour Biol.* 2012;33:669–677.
13. Pandit-Taskar N, O'Donoghue JA, Ruan S, et al. First-in-human imaging with <sup>89</sup>Zr-Df-IAB2M anti-PSMA minibody in patients with metastatic prostate cancer: pharmacokinetics, biodistribution, dosimetry, and lesion uptake. *J Nucl Med.* 2016;57:1858–1864.
14. Tove Olafsen ZKJ, Jason Romero, Charles Zamilpa, et al. Abstract LB-188: sensitivity of <sup>89</sup>Zr-labeled anti-CD8 minibody for PET imaging of infiltrating CD8+ T cells [abstract]. *Cancer Res.* 2016;76(14 suppl):LB-188.
15. Holland JP, Caldas-Lopes E, Divilov V, et al. Measuring the pharmacodynamic effects of a novel Hsp90 inhibitor on HER2/neu expression in mice using Zr-DFO-trastuzumab. *PLoS One.* 2010;5:e8859.
16. Holland JP, Divilov V, Bander NH, Smith-Jones PM, Larson SM, Lewis JS. <sup>89</sup>Zr-DFO-J591 for immunoPET of prostate-specific membrane antigen expression in vivo. *J Nucl Med.* 2010;51:1293–1300.
17. Holland JP, Sheh Y, Lewis JS. Standardized methods for the production of high specific-activity zirconium-89. *Nucl Med Biol.* 2009;36:729–739.
18. Morgan DJ, Bray KM. Lean body mass as a predictor of drug dosage: implications for drug therapy. *Clin Pharmacokinet.* 1994;26:292–307.
19. Reuben A, Spencer CN, Prieto PA, et al. Genomic and immune heterogeneity are associated with differential responses to therapy in melanoma. *NPJ Genom Med.* 2017;2:10.
20. Börjesson PK, Jauw YW, de Bree R, et al. Radiation dosimetry of <sup>89</sup>Zr-labeled chimeric monoclonal antibody U36 as used for immuno-PET in head and neck cancer patients. *J Nucl Med.* 2009;50:1828–1836.